communications earth & environment

Article

A Nature Portfolio journal

https://doi.org/10.1038/s43247-026-03312-6

Net primary productivity orchestrates uncertainty sources driving global soil organic carbon under land use change

Chengcheng Gang[1,2,3], Ning Wei[3] ✉, Chenxi Feng[3], Haodi Xu[3], Huanhuan Liu[4], Feng Tao[5], Lifen Jiang[3], Jianyang Xia[6], Stephen Sitch[7] & Yiqi Luo[3]

Land use and cover changes (LULCC) have profoundly influenced global soil organic carbon (SOC) stock, yet SOC responses to LULCC are among the largest but least quantified uncertainties in estimating land carbon emissions. Here we comprehensively estimated the LULCC-induced SOC changes over the past century using data from three widely recognized model inter-comparison projects. A refined multi-dimensional diagnostic framework was employed to dissect the underlying processes governing SOC changes following LULCC. Results revealed notable discrepancies among models. Despite varying magnitudes, soil carbon residence time consistently contributed negatively to LULCC-induced SOC changes. Conversely, net primary productivity (NPP)-driven SOC changes emerged as the largest source of uncertainty, predominantly fueling SOC gains in some model ensembles but depletion in others. Our findings underscore the need to better constrain simulated NPP and soil turnover processes to improve the accuracy of LULCC-induced SOC change predictions, pivotal for advancing global carbon management and climate mitigation strategies.

Soil represents the largest terrestrial carbon pool, containing nearly four times more carbon than vegetation biomass and three times more than the atmosphere[1,2]. Approximately two-thirds of this soil carbon exists as soil organic carbon (SOC), and even a minor fluctuation in SOC stock can significantly affect atmospheric concentrations of CO_2 and CH_4, thereby influencing the climate system[3,4]. The magnitude of SOC changes depends on the two main counterbalanced processes: carbon inputs from vegetation primary productivity and carbon outputs through microbial decomposition[5–7]. Land use and land cover change (LULCC) is considered the largest anthropogenic driver among a range of abiotic and biotic factors that influence these processes[8,9]. In recent decades, global LULCC has intensively affected about one-third of the worldwide land area[10]. Therefore, quantifying the responses of SOC to LULCC is crucial for advancing global climate mitigation strategies and ensuring sustainable soil management practices[10–13].

LULCC influences SOC stocks through multiple pathways, such as deforestation[14,15], cultivation[16], afforestation[17,18], and land management[19,20]. These activities substantially affect net primary productivity (NPP) by altering vegetation types, ecosystem structure, and resource availability. This, in turn, regulates carbon allocation to litter and soil pools and ultimately modulates soil decomposition[4,21]. For example, when forests are converted to croplands, the removal of litterfall, roots, and woody debris suppresses NPP and carbon inputs to the soil, leading to reduced SOC stock[8,11]. Deforestation in the Amazon has caused a sharp decrease in SOC following conversion from forest to cropland and pasture[22,23]. Typically, croplands are characterized by lower NPP and diminished litter input due to their shorter growing seasons compared to natural vegetation, coupled with a shortened soil carbon residence time driven by recurrent biomass removal through harvesting[16,19]. Moreover, intensive management practices, such as tillage, disrupt soil structure and expose SOC to oxidative processes. This accelerates decomposition rates and exacerbates carbon losses[19]. Over the past decade (2013–2022), global CO_2 emissions from land-use change, driven primarily by deforestation, were estimated at 1.3 ± 0.7 Gt C per year[3]. Conversely, extensive afforestation practices in China have enhanced soil carbon stock in natural ecosystems over recent decades by increasing NPP[17,24]. Thus, the multifaceted nature of LULCC exerts pervasive control

[1]College of Soil and Water Conservation Science and Engineering, Northwest A&F University, Yangling, China. [2]Institute of Soil and Water Conservation, Chinese Academy of Sciences and Ministry of Water Resources, Yangling, China. [3]School of Integrative Plant Science, Cornell University, Ithaca, NY, USA. [4]Key Laboratory of Ecosystem Network Observation and Modeling, Institute of Geographic Sciences and Natural Resources Research, Chinese Academy of Sciences, Beijing, China. [5]Department of Ecology and Evolutionary Biology, Cornell University, Ithaca, NY, USA. [6]Research Center for Global Change and Ecological Forecasting, School of Ecological and Environmental Sciences, East China Normal University, Shanghai, China. [7]Faculty of Environment, Science and Economy, University of Exeter, Exeter, UK. ✉e-mail: nw374@cornell.edu

on NPP, carbon allocation, and soil decomposition processes. Deciphering these interacting impacts is crucial for advancing process-based understanding of SOC dynamics under LULCC and addressing associated uncertainties.

Dynamic global vegetation models (DGVMs) are commonly used to simulate the long-term terrestrial carbon cycles and enable systematic partition of the influence of LULCC on model estimates of carbon stocks and fluxes[25–27]. Due to inherent differences in embedded assumptions, DGVMs typically manifest diverse structures and parameterizations[12,28]. Consequently, these models simulate different responses of SOC to LULCC. Harnessing ensembles of DGVMs with varying levels of complexities provides complementary perspectives to unravel terrestrial carbon dynamics and facilitate a more robust attribution of key processes governing SOC changes[25,29–31]. Among these, three widely recognized model intercomparison projects (MIPs)—the Multi-scale Synthesis and Terrestrial Model Intercomparison Project (MsTMIP), the Land Use Model Intercomparison Project (LUMIP), and the Trends and drivers of the regional scale terrestrial sources and sinks of carbon dioxide (TRENDY)—represent major coordinated initiatives developed over recent decades to advance our understanding of LULCC impacts on biogeochemical cycles[3,25,32]. These MIPs encompass distinct structural frameworks, forcing datasets, and the representation of climate–carbon feedback. While MsTMIP and TRENDY both rely on prescribed climate forcing, with TRENDY incorporating updated land-use transitions and an expanded ensemble of DGVMs, LUMIP employs coupled Earth System Models (ESMs) that allow interactive land–atmosphere feedbacks[3,4,26,32].

Recent multi-model ensemble results demonstrated that SOC change driven by LULCC was one of the largest sources of uncertainty regarding both directions and magnitudes[12,26,33]. The large spread in SOC stock across models has further amplified uncertainties in LULCC-induced SOC projections, particularly at regional scales[4]. This discrepancy arises from several factors, including the quality of historical land use/cover maps, varying model structures, parameterization schemes, and boundary conditions used across models[3,12,34]. These limitations inevitably introduce uncertainties into simulations of carbon input and output processes.

Despite advances in modeling, uncertainties in LULCC-induced SOC projections remain large, as the underlying processes are still poorly quantified and often elusive[4]. This knowledge gap is particularly troubling, given the increasing importance of land management in future climate mitigation strategies. Projections are less reliable when key processes are inadequately represented. These insights make it imperative to pinpoint the primary determinants of uncertainty in DGVMs and to elucidate the intricate relationships between drivers and SOC dynamics across different spatial scales. By identifying these drivers that contribute to inter-model variance, we can better target aspects for model refinement. This holds significance in offering essential guidance for shaping policies related to carbon sequestration, sustainable land-use practices, and climate change mitigation.

In this study, we first analyzed simulated SOC from a suite of 35 DGVMs incorporated within three MIPs, including 12 models from MsTMIP, six ESMs from LUMIP (land components are DGVMs), and 17 models from TRENDY version 9 (TRENDYv9). These models provide paired simulations with and without LULCC, facilitating the quantification of LULCC-induced SOC dynamics since 1901. To capture spatiotemporal variability, the post-MIP diagnostic traceability framework was used to trace LULCC-induced SOC changes to different drivers, enabling a coherent comparison of uncertainty sources within and among MIPs at both global and regional scales. This study addresses the following three research questions: (1) What are the direction and magnitude of LULCC-induced SOC changes across and within the MIPs? (2) How do traceable processes contribute to these dynamics for model improvement? (3) Where do models consistently agree, and most importantly, disagree across MIPs regionally? (See "Methods").

Results and discussion

Spatial and temporal trajectories of LULCC-induced SOC changes across MIPs

The three MIPs exhibit notable discrepancies in the direction of LULCC-induced SOC changes. Specifically, the ensemble mean of LUMIP indicated that LULCC has persistently driven SOC accumulation since 1901, culminating in an increase of 27.1 ± 64.1 Pg C (Fig. 1a). In contrast, estimates from MsTMIP and TRENDYv9 ensembles indicated SOC depletion with 59.5 ± 109.6 Pg C and 25.1 ± 32.1 Pg C, respectively (Fig. 1a, b).

Within LUMIP, models including BCC-CSM2-MR, CNRM-ESM2-1, and CMCC-ESM2 all simulated consistent SOC gains following LULCC, with BCC-CSM2-MR showing the highest increase at 115.1 Pg C. Conversely, the most substantial decrease was simulated by MPI-ESM1-2-LR, amounting to 42.4 Pg C (Supplementary Fig. 1b). MsTMIP ensemble exhibited considerable temporal variation in LULCC-induced SOC losses, ranging from a sharp loss of −356.3 Pg C (JPL-CENTURY) to a moderate gain of 13.8 Pg C (SiBCASA) between 1901 and 2010 (Supplementary Fig. 1a). In TRENDYv9, all models showed negative impacts of LULCC on SOC (Fig. 1a), with YIBS simulating the largest decrease at 128.7 Pg C from 1901 to 2019. This reduction was two orders of magnitude greater than those

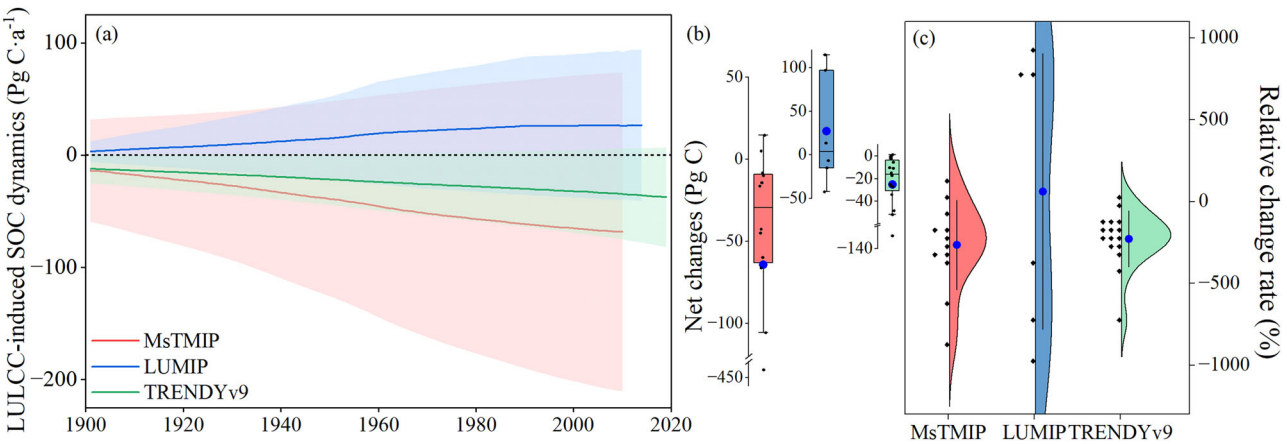

Fig. 1 | Temporal evolution and magnitude of LULCC-induced SOC dynamics across three MIPs. a The shaded area around the multi-model ensemble indicates mean ± 1 s.d., representing variability across models. **b** Blue dots mark the ensemble mean of net SOC changes (Unit: Pg C), and black dots represent net SOC changes for each individual model. **c** Blue dots indicate the ensemble mean of relative changes (%), and black dots show relative changes for each model, calculated as the percentage change in SOC relative to the without-LULCC baseline. Detailed temporal trends of LULCC-induced SOC changes for individual models within each MIP can be found in Supplementary Fig. 1.

simulated by CABLE, JULES, ISAM, LPJ-wsl, and LPX-Bern (Supplementary Fig. 1c). While LUMIP and TRENDYv9 imposed more stringent constraints, LUMIP exhibited greater variability in relative changes in LULCC-induced SOC across models, contrasting with the narrower spread observed in MsTMIP and TRENDYv9 (Fig. 1c). Notably, the consistently narrower uncertainty in TRENDYv9 for both net and relative changes (Fig. 1b, c) is likely related to its strict model selection protocol, which is not imposed in MsTMIP or LUMIP[3].

Spatially, LULCC exerted a global influence on SOC, with notable hotspots in the northern high latitude and tropical regions (Fig. 2a–c). The MsTMIP-based analysis demonstrated the most extensive latitudinal and spatial variations in LULCC-induced SOC changes (Supplementary Figs. 2 and 3). Overall, LULCC resulted in SOC loss across 67.3% of the global land area. The pronounced SOC reductions were observed in the central US, Europe, China, and southeastern South America (Fig. 2a). In contrast, the LUMIP-based multi-model mean indicated that LULCC contributed to SOC gains over 52.0% of the global land surface, with notable gains concentrated in the northern latitudes (Fig. 2b and Supplementary Fig. 4). Although exhibiting less latitudinal and spatial variabilities, the TRENDYv9 ensemble mean indicated that a larger portion (80.4%) of the global land area experienced SOC decrease due to LULCC. Notably, over 13 models consistently agreed that these regions were predominantly located in North America, Europe, Asia, South America, and Africa (Fig. 2c and Supplementary Fig. 5).

At the regional scale, LUMIP-based estimates showed LULCC led to a SOC decrease only in SES (0.005 ± 0.02 Pg C yr^{-1}), and the most substantial increase was in the temperate region (0.1 ± 0.2 Pg C yr^{-1}). In contrast, LULCC contributed to SOC losses across all subregions in both MsTMIP- and TRENDYv9-based estimations (Fig. 2d). The model ensemble mean of MsTMIP indicated that SOC loss rates exceeding 0.05 Pg C yr^{-1} (~5.5 Pg C from 1901 to 2010) were observed in AF (0.08 ± 0.2 Pg C yr^{-1}), EAS (0.06 ± 0.1 Pg C yr^{-1}), MIDE (0.06 ± 0.1 Pg C/yr), SA (0.1 ± 0.2 Pg C yr^{-1}), and the USA (0.08 ± 0.2 Pg C yr^{-1}). The model ensemble mean of TRENDYv9 showed that SOC loss rates were uniformly below 0.05 Pg C yr^{-1}, with the highest loss rate in RU at 0.04 ± 0.07 Pg C yr^{-1} (Fig. 2d).

Despite some discrepancies, the ensemble means of MsTMIP and TRENDYv9 consistently indicate that the tropical region experienced the highest LULCC-induced SOC loss, estimated at 0.2 ± 0.4 Pg C yr^{-1} and 0.09 ± 0.10 Pg C yr^{-1}, respectively. The larger deforested area recorded in Hurtt_SYNMAP relative to LUH2v2 may partially account for the greater SOC loss observed in MsTMIP than TRENDYv9 (Supplementary Fig. 6). A previous study demonstrated that reduced carbon input, combined with poor nutrients and highly weathered soils, led to greater SOC loss following LULCC compared to boreal and temperate regions[4]. This susceptibility can also be attributed to higher temperatures and soil moisture regimes, which enhance decomposition rates and accelerate SOC depletion[35,36]. Furthermore, predominant clay-rich soils in the tropics provide less mineral protection and stabilization for SOC[37].

Attribution of LULCC-induced SOC changes at the global scale

To further investigate the substantial inter-model spread in LULCC-induced SOC estimates, a multi-dimensional diagnostic analysis was conducted to disentangle its underlying drivers. This framework partitions SOC changes following LULCC into four structural drivers—carbon input (via NPP, $\Delta NPP^{*}\tau_{S0}$), decomposition (represented by soil residence time (τ_S, $\Delta\tau_S{}^{*}NPP_0$), their interactions ($\Delta NPP^{*}\Delta\tau_S$), and disequilibrium magnitude (ΔX_P)—for each model across the three MIPs (see "Methods").

NPP acts as a pivotal nexus between LULCC and SOC, where alterations in vegetation productivity directly modulate the balance between carbon inputs and outputs. Conventionally, land conversions such as deforestation and cultivation have been associated with declines in NPP[8,11,38]. From 1901 to the 2010s, both Hurtt_SYNMAP and LUH2v2, albeit with discrepancies, agree on persistent cropland expansion at the expense of forests at the global scale (Supplementary Fig. 6). However, NPP responded inconsistently to these processes across models.

The model ensemble means of MsTMIP and TRENDYv9 both revealed that NPP-driven SOC exerted a negative influence on SOC changes following LULCC since the 1900s. In the MsTMIP ensemble, NPP-driven SOC accounted for approximately 40% of the total LULCC-induced SOC loss, exhibiting only minor temporal fluctuations since the 1940s ($\Delta C^{MsTMIP}_{LULCC-SOC}|_{\Delta NPP^{*}_{\tau_{S0}}} = -27.9 \pm 44.5$ Pg C in the 2010s, Fig. 3a). Marked

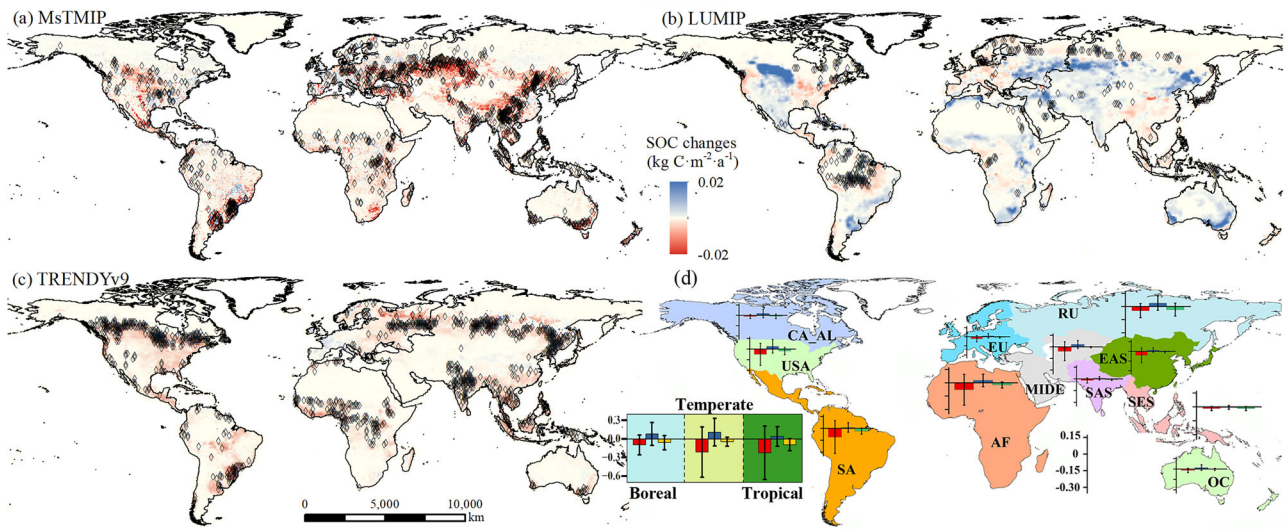

Fig. 2 | Spatial patterns of multi-model ensemble mean of LULCC-induced SOC changes. a–c Indicate the spatial dynamics of the ensemble mean of LULCC-induced SOC for MsTMIP, LUMIP, and TRENDYv9, respectively (Unit: kg C m^{-2}). The diamond symbols denote regions where more than 70% of models concur on the change direction within each MIP. Detailed spatial dynamics of LULCC-induced SOC for individual models in each MIP are presented in Supplementary Figs. 3–5. All three panels share the same figure legend. **d** Multi-model ensemble mean of LULCC-induced SOC changes in the 11 sub-regions and three climate zones (mean ± sd, Unit: Pg C yr^{-1}). Red, blue, and orange bars represent the MsTMIP, LUMIP, and TRENDYv9 ensemble, respectively. The 11 subregions include CA_AL (Canada and Alaska), USA, SA (Latin America and the Caribbean), AF (Africa), EU (Europe), RU (Russia), MIDE (Middle East), SAS (South Asia), SES (Southeast Asia), EAS (East Asia), and OC (Oceania). The boreal region (light blue background) encompasses CA_AL, EU, and RU, while the temperate region (light green background) comprises USA, MIDE, EAS, and OC. The tropical region (green background) consists of AS, AF, SAS, and SES.

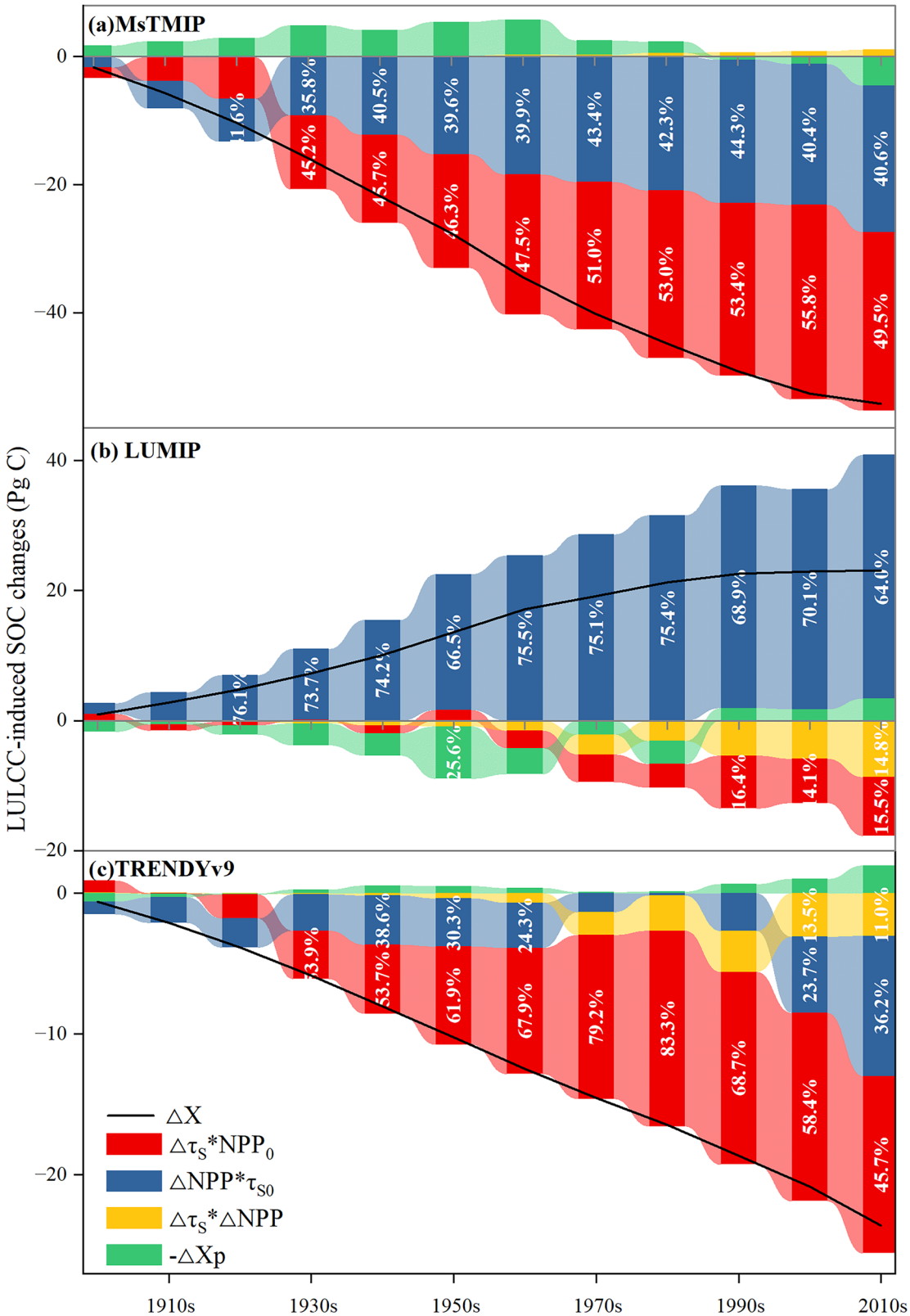

Fig. 3 | Temporal trends of the four processes in driving LULCC-induced SOC changes for three MIPs (Unit: Pg C). Temporal trends in driver attributions to the multi-model ensemble mean, derived from MsTMIP (**a**), LUMIP (**b**), and TRENDYv9 (**c**). The contributions are divided into four parts, including τ_S ($\Delta\tau_S$*NPP_0, shown in red color), NPP (ΔNPP*τ_{S0}, shown in blue color), their interaction (ΔNPP*$\Delta\tau_S$, shown in yellow color), and disequilibrium magnitude (ΔX_P, shown in green color). Black lines represent total LULCC-induced SOC changes. Percentages shown on the bars indicate the proportional contributions of each factor, quantified by normalizing the absolute magnitude of its contribution to the sum of absolute contributions from all drivers (<10% are not shown). Temporal trends for the four driving factors in each model within an MIP were provided in Supplementary Figs. 7–9.

inter-heterogeneity was observed within MsTMIP, with the impact of NPP spanning from −242.7 Pg C in JPL-CENTURY to 113.1 Pg C in ORCHIDEE-LSCE (Supplementary Fig. 7). In contrast, the contribution of NPP-driven contribution in TRENDYv9 was considerably weaker than that in MsTMIP, rarely exceeding 30% since the 1910s and falling below 10% during the 1970s–1990s. While exhibiting a narrower range, its inter-model variability surpassed that observed in MsTMIP ($\Delta C^{TRENDYv9}_{LULCC-SOC}|_{\Delta NPP^*\tau_{S0}}$ = −9.95 ± 34.4 Pg C in the 2010s, Fig. 3c). Conversely, the LUMIP ensemble attributed the increase in LULCC-induced SOC predominantly to rising NPP, which contributed ~70% since the 1930s ($\Delta C^{LUMIP}_{LULCC-SOC}|_{\Delta NPP^*\tau_{S0}}$ = 37.5 ± 49.7 Pg C in the 2010s, Fig. 3b and Supplementary Fig. 8). Within LUMIP, the elevated NPP dominated the rising LULCC-induced SOC in BCC-CSM2-MR, CMCC-ESM2, and CNRM-ESM2-1. Positive contributions from NPP were also evident in IPSL-CM6A-LR and UKESM1-0-LL. However, these gains were counterbalanced by the reduction in τ_S-driven changes, ultimately leading to a net SOC decline (Supplementary Fig. 8).

The discrepancies in NPP-driven SOC responses to LULCC could be ascribed to multiple structural factors. First, DGVMs in LUMIP allow for stronger feedback between carbon cycles and climate variations, while those in MsTMIP and TRENDYv9 use prescribed climate forcing[25,26,32]. These varying climate model representations within the LUMIP ensemble may introduce extra bias in LULCC-induced NPP changes[29,39]. Furthermore, the interplay between climate and LULCC in LUMIP may further amplify the CO_2 fertilization effect on SOC dynamics, leading to divergent model responses[40]. Second, some models utilize a single plant functional type (PFT) per grid cell, while others adopt a cohort strategy that incorporates multiple PFTs within the same grid[12]. The number of PFT types varies across DGVMs, even when adhering to identical simulation protocols within an MIP. Third, land-use trajectories often differ due to varying rules for modeling the expansion or abandonment of cropland in DGVMs[41]. Certain models assume that changes in cropland area result in a proportional reduction or expansion of existing natural PFTs within the grid[42,43]. Some other models apply preferential adjustments, such as reducing or expanding grassland for pasture, proportionally altering natural PFTs for cropland, or reallocating grassland for both cropland and pasture[44,45]. These varying allocation strategies for the compensating cropland area inevitably lead to divergent LULCC histories, which, in turn, result in different historical SOC dynamics induced by LULCC.

The inter-model variability in τ_S reflects differences in soil turnover and associated parameters[31]. The three MIPs broadly concurred that τ_S-driven changes negatively impacted LULCC-induced SOC dynamics. The ensemble mean of MsTMIP indicated that τ_S-driven SOC loss marginally exceeded that attributable to NPP-driven changes since the 1900s, exhibiting minor fluctuations throughout the study period ($\Delta C^{MsTMIP}_{LULCC-SOC}|_{\Delta\tau S^* NPP_0}$ = −22.9 ± 83.7 Pg C in the 2010s, Fig. 3a). Conversely, the TRENDYv9 ensemble attributed the LULCC-induced SOC decline primarily to the τ_S-driven term, accounting for up to 83.3% during the 1980s, but diminishing thereafter ($\Delta C^{TRENDYv9}_{LULCC-SOC}|_{\Delta\tau S^* NPP0}$ = −12.6 ± 17.7 Pg C in the 2010s, Fig. 3c). The contribution of τ_S-driven changes varied substantially across models, ranging from −42.7 Pg C in YIBS to 14.6 Pg C in CABLE. Notably, in the TRENDYv9 ensemble, NPP and τ_S demonstrated distinct yet counterbalancing roles in shaping LULCC-induced SOC changes, which nonetheless exhibited similar temporal trends. This interplay was particularly evident in JULES, CABLE, LPX-Bern, and ISAM (Supplementary Fig. 9). In contrast, although τ_S-driven SOC contributions increased from the 1910s onwards, their impact remained relatively modest in LUMIP, accounting for only ~15% of LULCC-induced SOC changes after the 1990s (Fig. 3b). All MIPs agreed that the interactions between NPP and residence time ($\Delta NPP^*\Delta\tau_S$), as well as the disequilibrium magnitude (ΔX_P), had minimal contributions to SOC changes throughout the study period (Fig. 3).

Quantitatively attributing changes in soil residence time to SOC dynamics remains an intricate challenge. This complexity arises partly from the prevalent reliance of most current DGVMs on first-order kinetics to estimate cascading decomposition rates among soil carbon pools[28,46], which inadequately represent microbial-related processes like priming effects that regulate carbon accumulation and turnover[47,48]. Moreover, models exhibit substantial heterogeneity in their representation of soil carbon pools: while some adopt simplified multi-pool configurations, others integrate microbial dynamics, freeze–thaw cycles, or vertical carbon transport, resulting in markedly divergent τ_S responses to comparable land conversions[3,12,25,26]. Furthermore, disturbances and management practices—such as fire frequency, wood harvest intensity, and fertilization—are also prescribed differently across MIPs, either amplifying or mitigating SOC losses in specific regions[12,27,29]. Additionally, differences in spin-up protocols and historical baselines may influence the initial SOC stock and the legacy effects of past land-use changes[26]. Collectively, these structural divergences propagate through model ensembles, contributing substantially to the inter-model spread in τ_S-driven SOC estimates.

The contributions of the four components to LULCC-induced SOC changes exhibited large spatial variability, as reflected in the ensemble mean of each MIP (Fig. 4). All three MIPs consistently showed that τ_S-driven

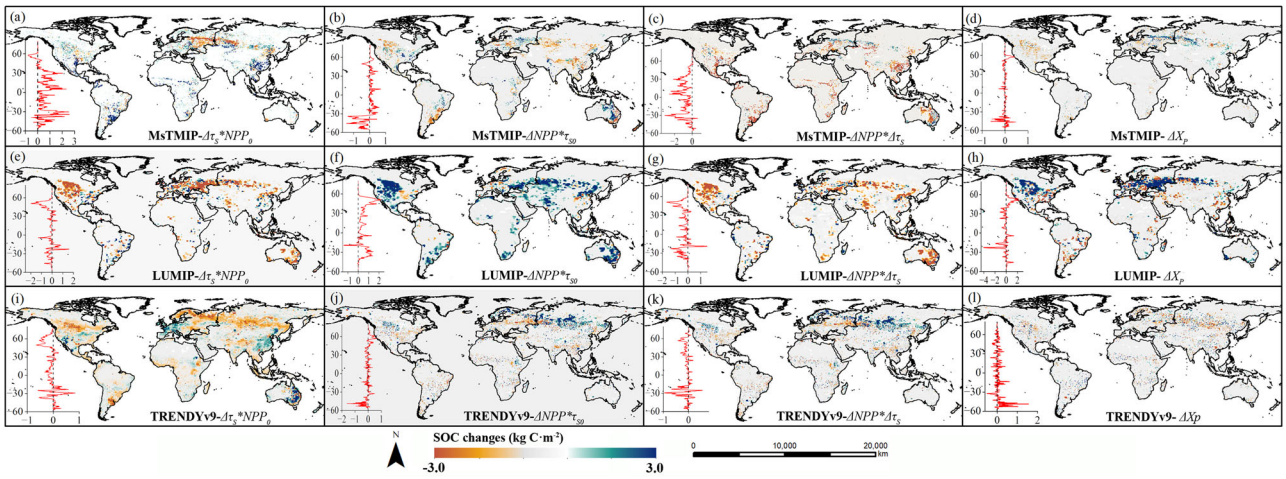

Fig. 4 | Spatial patterns of dominant process contributions in driving LULCC-induced SOC changes during the 2010s (Unit: kg C m^{-2} a^{-1}). Spatial patterns of the contributions from τ_S ($\Delta\tau_S$*NPP_0), NPP ($\Delta NPP^*\tau_{S0}$), their interaction ($\Delta NPP^*\Delta\tau_S$), and disequilibrium magnitude (ΔX_P) in driving LULCC-induced SOC changes during the 2010s (Unit: kg C m^{-2}). Results are derived from the multi-model ensemble mean for MsTMIP (**a** MsTMIP-$\Delta\tau_S$*NPP_0; **b** MsTMIP-$\Delta NPP^*\tau_{S0}$; **c** MsTMIP-$\Delta NPP^*\Delta\tau_S$; **d** MsTMIP-ΔX_P), LUMIP (**e** LUMIP-$\Delta\tau_S$*NPP_0; **f** LUMIP-$\Delta NPP^*\tau_{S0}$; **g** LUMIP-$\Delta NPP^*\Delta\tau_S$; **h** LUMIP-ΔX_P), and TRENDYv9 (**i:** TRENDYv9-$\Delta\tau_S$*NPP_0; **j** TRENDYv9-$\Delta NPP^*\tau_{S0}$; **k** TRENDYv9-$\Delta NPP^*\Delta\tau_S$; **l** TRENDYv9-ΔX_P). The inset panels illustrate the latitudinal mean of each driver (Unit: kg C m^{-2} a^{-1}).

changes were concentrated in northern high latitudes. In MsTMIP, its negative impact was confined to central Eurasia (Fig. 4a). Conversely, in LUMIP and TRENDYv9, τ_S-driven changes were broadly distributed across North America, Europe, and Asia, with a much larger affected area in TRENDYv9 (Fig. 4e, i). It is noteworthy that the positive impact of τ_S in western Europe and eastern Australia, evident in TRENDYv9, was absent in both MsTMIP and LUMIP (Fig. 4i). The positive contribution of NPP to SOC changes following LULCC was particularly pronounced in LUMIP (Fig. 4f), while in MsTMIP and TRENDYv9, its effects were scattered across the northern high latitudes, with limited impact observed in Asia (Fig. 4b, j). Despite some differences, both Hurtt_SYNMAP and LUH2v2 consistently showed that cropland areas in the western US expanded steadily from 1901, peaked around the 1960s, and declined thereafter. The forest area exhibited the opposite trend over the same period (Supplementary Fig. 6). However, modeled NPP demonstrated inter-model variation within and across the MIPs. Increment in NPP-driven SOC was observed in 7, 3, and 6 models from MsTMIP, LUMIP, and TRENDYv9, respectively (Supplementary Figs. 10 and 11).

Key processes driving LULCC-induced SOC changes at the regional scale

The regional-scale analysis offers comprehensive insights into how the four determinants contributed differently to LULCC-induced SOC changes (Fig. 5). In boreal regions, the observed rise in LULCC-induced SOC within LUMIP was predominantly attributed to increases in NPP- and X_P-driven changes, partially counterbalanced by reductions in τ_S over the study period. Both MsTMIP and TRENDYv9 ensembles indicated that decreases in NPP were the primary drivers of LULCC-induced SOC reduction in CA_AL and RU, with comparable magnitudes (Fig. 5a, c). In Europe, while both the two MIPs identified a negative influence of τ_S, NPP-driven changes contributed to an overall SOC decrease in MsTMIP but reversed the reduction in TRENDYv9 (Fig. 5b). Since the 1950s, Europe has experienced widespread afforestation of former cropland[49]. In TRENDYv9, the ensemble mean of NPP exhibited an overall increasing trend, even though nine models indicated a decrease in NPP (Supplementary Fig. 10b). Nevertheless, the lag effect from persistently declining τ_S still led to SOC loss[5]. Previous studies highlighted that current DGVMs tend to underestimate soil carbon turnover time, especially in northern high latitudes by inadequately representing the permafrost process[29,39,50]. Therefore, the contribution of τ_S-driven SOC loss following LULCC is likely underestimated in the current estimation of MsTMIP and TRENDYv9.

LULCC in temperate regions has been characterized by both intensification and extensification over the last decades[5]. We found that the processes driving SOC changes exhibited more substantial disparities among the MIPs. According to LUMIP estimations, NPP played a prominent role in driving the LULCC-induced SOC increase across these four subregions (Fig. 5d–g and Supplementary Fig. 11). Conversely, the ensemble means of MsTMIP and TRENDYv9 broadly concur that deforestation led to declines in NPP and τ_S in USA, MIDE, and OC, subsequently causing SOC loss (Supplementary Fig. 11a, c, d). The greater reduction in forest area captured by Hurtt_SYNMAP, used in MsTMIP, may explain the larger SOC loss compared to TRENDYv9, which uses LUH2v2 as land use input (Supplementary Fig. 6). In EAS, NPP was the dominant contributor to SOC loss in MsTMIP ($\Delta C^{MsTMIP}_{LULCC-SOC}|_{\Delta NPP^*_{\tau_{S0}}} = -5.7 \pm 14.6$ Pg C), while it exhibited a positive contribution in TRENDYv9 ($\Delta C^{TRENDYv9}_{LULCC-SOC}|_{\Delta NPP^*_{\tau_{S0}}} = 2.8 \pm 11.3$ Pg C), counteracting the overall decline driven by the other three factors (Fig. 5e). Forest area consistently decreased in both Hurtt_SYNMAP and LUH2v2, declining more slowly in the former and reversing to an increase in the latter after the late 1980s. This may explain the noticeable positive trend in NPP in the TRENDYv9-based estimation. Although nine models simulated a reduction in NPP, these decreases were largely offset by the positive impacts of ORCHIDEEv3, LPJ-GUESS, and CLM5 (Supplementary Fig. 11b). In MsTMIP, the large model spread in SOC changes following LULCC was primarily attributed to the substantial decreases in NPP modeled by LPJ-CENTURY and JPL-HYLAND (Supplementary Fig. 11b).

Over the past century, rapid deforestation has occurred across the tropics to satisfy the growing demand for logging and agricultural land (Supplementary Fig. 6)[51]. Nonetheless, an NPP-driven increase in LULCC-induced SOC was prevalent across SA, AF, and SAS in LUMIP (Fig. 5h–j and Supplementary Fig. 12a). Although SOC decreased in SES (Fig. 5k), the

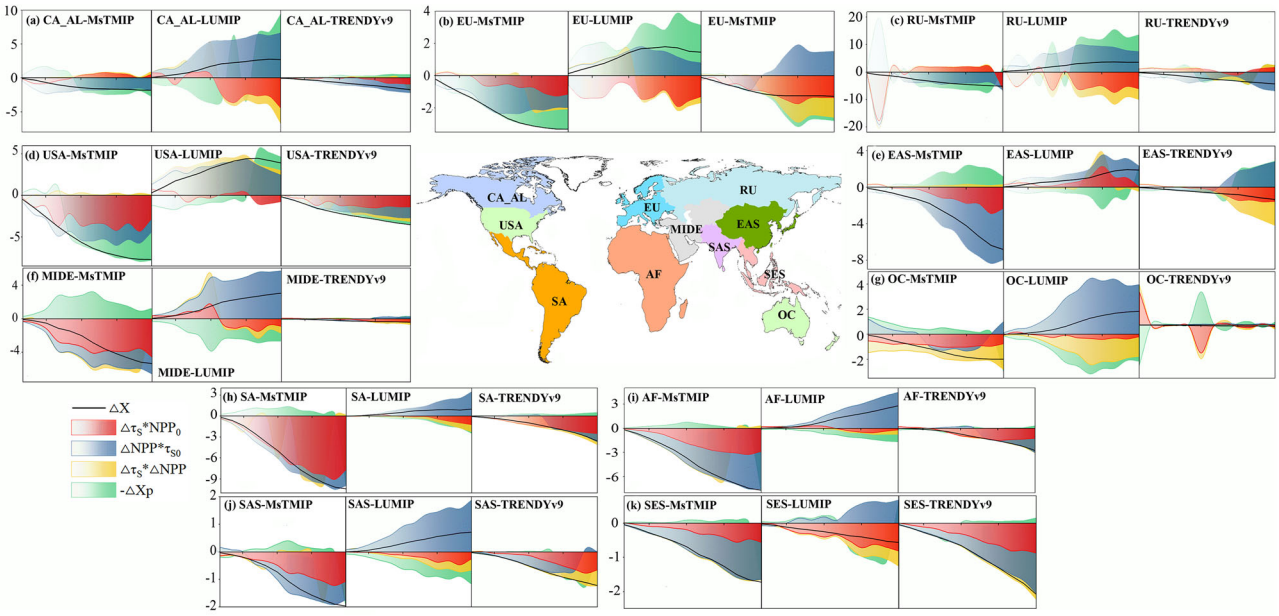

Fig. 5 | Temporal evolution of process contributions to LULCC-induced SOC changes at regional scales (Unit: Pg C). Temporal evolution of contributions from τ_S ($\Delta\tau_S{*}NPP_0$), NPP ($\Delta NPP{*}\tau_{S0}$), their interaction ($\Delta NPP{*}\Delta\tau_S$), and disequilibrium magnitude (ΔX_P) to LULCC-induced SOC changes across 11 subregions. For each subregion, the left, middle, and right panels correspond to estimates from MsTMIP, LUMIP, and TRENDYv9, respectively. Black lines represent the temporal trends in LULCC-induced SOC changes. Subregions include: **a** CA_AL: Canada and Alaska; **b** EU: Europe; **c** RU: Russia; **d** USA; **e** MIDE: Middle East region; **f** EAS: East Asia; **g** OC: Oceania; **h** SA: Latin America and the Caribbean; **i** AF: Africa; **j** SES: Southeast Asia; **k** SAS: South Asia.

positive effect of NPP was just slightly lower but comparable to τ_S ($\Delta C^{LUMIP}_{LULCC-SOC}|_{\Delta NPP^*_{\tau_{S0}}} = 0.7$ Pg C *vs.* $\Delta C^{LUMIP}_{LULCC-SOC}|_{\Delta\tau_S{}^* NPP_0} = -0.8$ Pg C). In SA, both MsTMIP and TRENDYv9 identified τ_S as the dominant factor shaping LULCC-induced SOC loss, whereas in SES, they consistently attributed the overall SOC decrease to the contributions of τ_S and NPP (Fig. 5h, k). In AF and SAS, the moderate contributions of NPP to LULCC-induced SOC observed in MsTMIP were absent in TRENDYv9 (Fig. 5i, j).

Evidence from incubation studies and model estimations indicates that tropical biomes have shorter soil carbon residence times than boreal and temperate ecosystems[29,39]. This pattern is primarily due to the detrimental effects of high temperature on residence time and shifts in microbial community composition[39,52]. For ecosystems, croplands typically exhibit shorter soil residence times owing to frequent human interference[53]. Consequently, the extensive deforestation for cropland expansion, particularly in the tropical regions, over the past century, is presumed to have considerably reduced global soil residence time[54,55]. It is noteworthy that the representation of cropland has undergone successive updates, evolving from Hurtt_SYNMAP to LUH-GCB2020 through inventory-based corrections and satellite-derived observations[56,57]. Nevertheless, pronounced discrepancies persist in forests and grasslands, particularly at regional scales, due to differing treatments of natural vegetation across simulation protocols[11,25,32]. For example, forest area trajectories in SA differed substantially between Hurtt_SYNMAP and LUH2v2, which likely amplified the regional spread of τ_S-driven SOC changes (Supplementary Fig. 6).

A key challenge in accurately quantifying LULCC-induced SOC dynamics lies in the lack of long-term, spatially explicit observations that can separate land-use signals from other concurrent drivers, such as climate variability and management practices. Existing global SOC inventories provide valuable insights but are typically restricted to recent decades and exhibit substantial regional inconsistencies, posing particular limitations for century-scale analyses[5,11,13]. Direct observations of NPP and τ_S over such extended periods are even more elusive due to the inherent spatiotemporal constraints of conventional field methodologies. Although satellite-derived NPP products deliver high-resolution insights into vegetation productivity, their temporal span is largely confined to the post-2000 era, and τ_S estimates remain predominantly model-based due to the difficulty of direct measurements[29,31,39]. This persistent observational gap constrains the calibration and benchmarking of DGVMs in capturing both carbon inputs and turnover under historical and ongoing land-use changes.

Addressing these constraints requires multifaceted strategies. First, integrating high-resolution satellite products with historical reconstructions, such as climate proxies, can improve data continuity and spatial resolution. Second, establishing comprehensive global observation networks should prioritize underrepresented boreal regions. These networks should integrate extensive soil-sampling campaigns with long-term standardized field experiments (e.g., multi-site incubation studies) to provide essential benchmarks for constraining and validating NPP and τ_S in models. Advances in remote sensing, particularly emerging missions capable of retrieving vegetation productivity and belowground carbon proxies, offer valuable opportunities to inform and calibrate model parameterizations. Furthermore, leveraging artificial intelligence, such as Knowledge Guided-Machine Learning (KGML), holds great potential to bridge the gap by assimilating heterogeneous datasets (e.g., remote sensing, inventories, eddy covariance) into process-based models. Such data–model fusion approaches can dynamically optimize parameters related to NPP allocation, soil turnover, and disturbance regimes, while enhancing interpretability by establishing causal linkages across variables. Embedding these AI-driven integration techniques within model intercomparison frameworks, future studies could enable more robust and spatially resolved estimates of LULCC-induced SOC dynamics, ultimately reducing inter-model disparities, enhancing global carbon budget predictions, and informing precise climate mitigation strategies.

In summary, this study provides a comprehensive, process-oriented attribution of LULCC-induced SOC dynamics across three widely recognized MIPs through post-MIP traceability, a distinct multi-dimensional diagnostic framework. Our findings reveal substantial uncertainties with respect to the directions and magnitudes of SOC changes, spanning both across and within the MIPs. Three MIPs concurred that the reduced soil residence time drove LULCC-induced SOC loss, albeit to varying degrees. In contrast, the contribution of NPP to SOC dynamics remained highly contentious, orchestrating the dominant uncertainty underlying the substantial divergences across the MIPs. In this regard, achieving more reliable projections of LULCC-induced SOC dynamics requires tighter tethering of NPP and soil residence time responses to land conversions. This could be facilitated by improving observational constraints and harnessing emerging data–model fusion techniques to refine key parameters governing vegetation productivity and carbon turnover, particularly in the boreal region. These advancements are vital to bolster DGVMs, thereby enhancing carbon sink predictions for global climate mitigation strategies.

Methods

MsTMIP ensemble

Given the available datasets, twelve model outputs were used in the analysis, including CLASS-CTEM-N+, CLM4, DLEM, GTEC, JPL-HYLAND, ISAM, LPJ-wsl, JPL-CENTURY, ORCHIDEE-LSCE, SiBCASA, VEGAS, and VISIT. Model-specific details are provided in Supplementary Table 1.

These models were driven by benchmark reference driver data sets. Climate inputs were sourced from the 6-hourly CRU-NCEP dataset. The models were also forced by atmospheric CO_2, gridded nitrogen deposition, and remotely sensed phenology. Land use/cover was prescribed by merging SYNMAP with the time-varying land use harmonization data (LUH) from the Fifth Assessment Report (AR5) of the Intergovernmental Panel on Climate Change (IPCC)[56,58]. LUH provides mapped fractional coverage and annual transitions for different land-use classes, including primary land, secondary land, cropland, pasture, urban, and barren. Global simulations were performed at 0.5° × 0.5° resolution, covering all land areas excluding Antarctica.

To separate the impact of LULCC on SOC, model outputs from two pair simulations, SG1 and SG2, were analyzed. SG1 incorporated time-varying climate forcing and land use change alongside constant atmospheric CO_2 and nitrogen deposition, while SG2 held constant land use change, aligning other forcings consistent with SG1. The differences between them can be considered the LULCC effect.

LUMIP ensemble

Six ESMs with distinct land-surface modules were analyzed in this study, including BCC-CSM2-MR, CMCC-ESM2, CNRM-ESM2-1, IPSL-CM6A-LR, MPI-ESM1-2-LR, and UKESM1-0-LL. Detailed information for each model is provided in Supplementary Table 2.

LUMIP employed the LUH2v2 as the land use/cover input dataset, while LULCC was depicted differently across land models. Some models utilized annual land-use maps as direct inputs, whereas others relied on transition matrices describing fractional changes between land-use types, leading to variations in how land conversions were prescribed and implemented[32].

We analyzed outputs from two simulations, *Land-hist* and *Land-noLu*, to estimate LULCC impacts on SOC. Both simulations were driven by transient forcings, including atmospheric CO_2, N-deposition, aerosol deposition, etc. Their difference lies in the *Land-hist* adopting the time-varying land use change as input, whereas *Land-noLu* held land use constant since 1850[32]. In this study, both *cSoil* and *cLitter* were accounted as the total soil carbon pool when available[26].

TRENDYv9 ensemble

This study analyzed outputs from 17 DGVMs participating in TRENDYv9, including CABLE, CLASSIC, CLM5, DLEM, IBIS, ISAM, JSBACH, JULES, LPJ-GUESS, LPJ-wsl, LPX-Bern, ORCHIDEEv3, OCN, ORCHIDEE-CNP, SDGVM, VISIT, and YIBS (see Supplementary Table 3 for detailed information).

These models were driven by merged climate data from the Climate Research Unit (CRU) and 6-hourly Japanese Reanalysis (JRA-55), along with gridded nitrogen deposition, nitrogen fertilizer, and atmospheric CO_2, adhering to consistent spin-up and historical simulations protocols[59,60]. TRENDYv9 utilized LUH-GCB2020 as land use input data, which contains updated woody harvest data from 2015 onwards[57].

To isolate the impact of LULCC on SOC, we used the model outputs from simulations S2 and S3. Both simulations share the same forcings, with S2 using fixed pre-industrial land-use and S3 adopting time-varying land use. Their difference reflects the impact of LULCC on SOC.

Post-MIP traceability framework

To systematically investigate the processes driving LULCC-induced SOC changes across multiple models, we developed a multi-dimensional diagnostic analysis within the post-MIP traceability framework. This analysis integrates spatial, temporal, and driver-specific dimensions to decompose SOC variations, leveraging a multi-model ensemble from the three MIPs.

The capacity of an ecosystem to store carbon is governed by two primary processes: carbon input, represented by NPP, and carbon residence time (τ)[4,31,61,62]. NPP and τ determine the carbon storage capacity (X_C) at a steady state, which represents the maximum attainable carbon storage within the ecosystem, where influx equals outflux[28,63]:

$$X_C = NPP^{*}\tau \tag{1}$$

In reality, however, terrestrial ecosystems frequently diverge from this steady state due to climate change and various disturbances[28,64]. To capture this deviation, a novel metric, X_P, was introduced to measure the extent of carbon storage departure from equilibrium conditions. Consequently, carbon storage in a transient state can thus be expressed as follows:

$$X = NPP^{*}\tau - X_P \tag{2}$$

The X_P is proportional to the rate of carbon storage change (X') and regulated by the chasing time τ_{ch}:

$$X_P = \tau_{ch}{}^{*}X' \tag{3}$$

For the soil carbon pool, changes in the soil carbon pool can be calculated as:

$$X = \tau_S{}^{*}(NPP - X') \tag{4}$$

Then, τ_S and X_P can be further calculated as:

$$\tau_S = \frac{X}{NPP - X'} \tag{5}$$

$$X_P = \tau_S{}^{*}NPP - X' \tag{6}$$

where (NPP- X') represents the total soil carbon losses from the terrestrial ecosystem, mainly through heterotrophic respiration and disturbances (i.e., fire, winds, and insects)[62,65].

Changes in soil carbon storage over a specific period can be expressed as:

$$\Delta X = \Delta X_C - \Delta X_P \tag{7}$$

where ΔX denotes the variation in the soil carbon pool over a certain period. ΔX_C represents changes in soil carbon storage capacity, while ΔX_P captures the changes in the disequilibrium amount over the same period. Given X_C is determined by NPP and τ_S, ΔX_C can therefore be substituted as follows:

$$\Delta X_C = (NPP_0 + \Delta NPP)^{*}(\tau_{S0} + \Delta\tau_S) - NPP_0{}^{*}\tau_{S0} \tag{8}$$

$$X_C = \Delta\tau_S{}^{*}NPP_0 + \Delta NPP^{*}\tau_{S0} + \Delta NPP^{*}\Delta\tau_S \tag{9}$$

where ΔNPP *and* $\Delta\tau_S$ are changes in NPP and τ_S relative to their initial values. After combining them with Eq. 7, it can be reformulated as follows:

$$\Delta X = \Delta\tau_S{}^{*}NPP_0 + \Delta NPP^{*}\tau_{S0} + \Delta NPP^{*}\Delta\tau_S - \Delta X_P \tag{10}$$

In this equation, the first term ($\Delta\tau_S{}^{*}NPP_0$) represents the soil carbon pool changes driven solely by the evolving τ_S, with NPP held constant. The second term ($\Delta NPP^{*}\tau_{S0}$) reflects shifts in the soil carbon pool attributable to variations in NPP. The third term ($\Delta NPP^{*}\Delta\tau_S$) represents the synergistic impact of simultaneous changes in both NPP and τ_S on carbon dynamics. These three components together determine the alteration in carbon storage capacity at a steady state. The final term (ΔX_P) addresses changes in the disequilibrium magnitude. Here, NPP_0 and τ_{S0} are historical reference values, calculated as the average from 1901 to the latest available year for each model. ΔNPP, $\Delta\tau_S$, and ΔX_P represent deviations from their historical baselines.

To quantify the impacts of the four components on LULCC-induced SOC, we first computed global SOC (including the litter carbon pool where available) and NPP under with- and without LULCC scenarios for each model across the three MIPs. The LULCC-induced SOC and NPP were calculated as the difference between a simulation with and one without land use. Then, ΔX was calculated for both scenarios across all models. Their differences in the aforementioned four terms were then interpreted as their respective contributions to LULCC-induced SOC changes. These contributions were assessed at decadal intervals (e.g., 1901–1910 as the 1900s, 1911–1920 as the 1910s, etc.) to compare the temporal evolution of the four components across MIPs. The proportional attribution of each driver was quantified based on the absolute contribution relative to the sum of absolute contributions from all drivers.

The spread of the model estimate of changes in SOC was used to determine the variability among simulations. For $\Delta C_{LULCC\text{-}SOC}$, we show the mean ± s.d., which reflects the inter-model spread within each MIP and primarily captures structural variability. The four diagnostic components driving LULCC-induced SOC dynamics were calculated for each model. Their respective statistics were subsequently derived as ensemble means with standard deviations within each MIP.

To facilitate regional-scale analysis, the global land area was subdivided into 11 subregions: CA_AL (Canada and Alaska), USA, SA (Latin America and the Caribbean), AF (Africa), EU (Europe), RU (Russia), MIDE (Middle East), SAS (South Asia), SES (Southeast Asia), EAS (East Asia), and OC (Oceania). For broader interpretation, these subregions were grouped into three climatic zones: the boreal region (CA_AL, EU, RU), the temperate region (USA, MIDE, EAS, OC), and the tropical region (SA, AF, SAS, SES).

Reporting summary

Further information on research design is available in the Nature Portfolio Reporting Summary linked to this article.

Data availability

The Hurtt-SYNMAP land-use dataset used in MsTMIP is provided by the Oak Ridge National Laboratory Distributed Active Archive Center (ORNL DAAC, http://daac.ornl.gov). The LUH2v2 land-use dataset, utilized in LUMIP and TRENDYv9, is available on the LUH2 website (https://luh.umd.edu). Raw model outputs for MsTMIP and LUMIP are publicly accessible online (MsTMIP: http://daac.ornl.gov; LUMIP: https://aims2.llnl.gov/search/ cmip6). TRENDY model outputs can be obtained upon request (https://globalcarbonbudgetdata.org/closed-access-requests.html). The post-processed data generated in this study are available at https://doi.org/10.5281/zenodo.14866783.

Received: 20 March 2025; Accepted: 9 February 2026;
Published online: 17 February 2026

References

1. Lal, R. Soil carbon sequestration impacts on global climate change and food security. *Science* **304**, 1623–1627 (2004).
2. Scharlemann, J. P. et al. Global soil carbon: understanding and managing the largest terrestrial carbon pool. *Carbon Manag.* **5**, 81–91 (2014).
3. Friedlingstein, P. et al. Global Carbon Budget 2023. *Earth Syst. Sci. Data* **15**, 5301–5369 (2023).
4. O Sullivan, M. et al. Process-oriented analysis of dominant sources of uncertainty in the land carbon sink. *Nat. Commun.* **13**, 4781 (2022).
5. Poeplau, C. et al. Temporal dynamics of soil organic carbon after land-use change in the temperate zone–carbon response functions as a model approach. *Glob. Change Biol* **17**, 2415–2427 (2011).
6. Friend, A. D. et al. Carbon residence time dominates uncertainty in terrestrial vegetation responses to future climate and atmospheric CO_2. *Proc. Natl. Acad. Sci. USA* **111**, 3280–3285 (2014).
7. Rafique, R. et al. Divergent predictions of carbon storage between two global land models: attribution of the causes through traceability analysis. *Earth Syst. Dyn.* **7**, 649–658 (2016).
8. Smith, P. Land use change and soil organic carbon dynamics. *Nutr. Cycl. Agroecosyst.* **81**, 169–178 (2008).
9. Houghton, R. A. Carbon flux to the atmosphere from land-use changes: 1850–2005. *TRENDS: A Compendium of Data on Global Change. Carbon Dioxide Information Analysis Center, Oak Ridge National Laboratory, U.S. Department of Energy, Oak Ridge, Tenn., U.S.A*1850-2005 (2008).
10. Winkler, K. et al. Global land use changes are four times greater than previously estimated. *Nat. Commun.* **12**, 2501 (2021).
11. Gang, C. et al. Uncertainty in land use obscures global soil organic carbon stock estimates. *Agric. For. Meteorol.* **339**, 109585 (2023).
12. Tian, H. et al. Global patterns and controls of soil organic carbon dynamics as simulated by multiple terrestrial biosphere models: current status and future directions. *Glob. Biogeochem. Cycle* **29**, 775–792 (2015).
13. Deng, L. et al. Global patterns of the effects of land-use changes on soil carbon stocks. *Glob. Ecol. Conserv.* **5**, 127–138 (2016).
14. Bautista-Cruz, A. et al. Selection and interpretation of soil quality indicators for forest recovery after clearing of a tropical montane cloud forest in Mexico. *For. Ecol. Manage.* **277**, 74–80 (2012).
15. Petrenko, C. L. & Friedland, A. J. Mineral soil carbon pool responses to forest clearing in Northeastern hardwood forests. *Glob. Change Biol. Bioenergy* **7**, 1283–1293 (2015).
16. Huon, S. et al. Long-term soil carbon loss and accumulation in a catchment following the conversion of forest to arable land in northern Laos. *Agric. Ecosyst. Environ.* **169**, 43–57 (2013).
17. Chen, C. et al. China and India lead in greening of the world through land-use management. *Nat. Sustain.* **2**, 122–129 (2019).
18. Poeplau, C. & Don, A. Sensitivity of soil organic carbon stocks and fractions to different land-use changes across Europe. *Geoderma* **192**, 189–201 (2013).
19. de Oliveira, S. P. et al. Organic carbon and nitrogen stocks in soils of northeastern Brazil converted to irrigated agriculture. *Land Degrad. Dev.* **26**, 9–21 (2015).
20. Yu, Z. et al. Long-term terrestrial carbon dynamics in the Midwestern United States during 1850-2015: roles of land use and cover change and agricultural management. *Glob. Change Biol.* **24**, 2673–2690 (2018).
21. Hartley, A. J. et al. Uncertainty in plant functional type distributions and its impact on land surface models. *Remote Sens. Environ.* **203**, 71–89 (2017).
22. Fujisaki, K. et al. From forest to cropland and pasture systems: a critical review of soil organic carbon stocks changes in Amazonia. *Glob. Change Biol.* **21**, 2773–2786 (2015).
23. Rittl, T. F., Oliveira, D. & Cerri, C. E. P. Soil carbon stock changes under different land uses in the Amazon. *Geoderma Reg.* **10**, 138–143 (2017).
24. Tang, X. et al. Carbon pools in China's terrestrial ecosystems: new estimates based on an intensive field survey. *Proc. Natl. Acad. Sci. USA* **115**, 4021–4026 (2018).
25. Huntzinger, D. N. et al. The North American Carbon Program Multi-Scale Synthesis and Terrestrial Model Intercomparison Project – Part 1: Overview and experimental design. *Geosci. Model Dev.* **6**, 2121–2133 (2013).
26. Ito, A. et al. Soil carbon sequestration simulated in CMIP6-LUMIP models: implications for climatic mitigation. *Environ. Res. Lett.* **15**, 124061 (2020).
27. Yue, C. et al. Contribution of land use to the interannual variability of the land carbon cycle. *Nat. Commun.* **11**, 3170 (2020).
28. Luo, Y. & Weng, E. Dynamic disequilibrium of the terrestrial carbon cycle under global change. *Trends Ecol. Evol.* **26**, 96–104 (2011).
29. Carvalhais, N. et al. Global covariation of carbon turnover times with climate in terrestrial ecosystems. *Nature* **514**, 213–217 (2014).
30. Luo, Y. et al. Transient dynamics of terrestrial carbon storage: mathematical foundation and its applications. *Biogeosciences* **14**, 145–161 (2017).
31. Zhou, S. et al. Sources of uncertainty in modeled land carbon storage within and across three MIPs: diagnosis with three new techniques. *J. Clim.* **31**, 2833–2851 (2018).
32. Lawrence, D. M. et al. The Land Use Model Intercomparison Project (LUMIP) contribution to CMIP6: rationale and experimental design. *Geosci. Model Dev.* **9**, 2973–2998 (2016).
33. Garsia, A. et al. The challenge of selecting an appropriate soil organic carbon simulation model: a comprehensive global review and validation assessment. *Glob. Change Biol.* **29**, 5760–5774 (2023).
34. Arneth, A. et al. Historical carbon dioxide emissions caused by land-use changes are possibly larger than assumed. *Nat. Geosci.* **10**, 79–84 (2017).
35. Don, A., Schumacher, J. & Freibauer, A. Impact of tropical land-use change on soil organic carbon stocks–a meta-analysis. *Glob. Change Biol.* **17**, 1658–1670 (2011).
36. Wang, J. et al. Soil and vegetation carbon turnover times from tropical to boreal forests. *Funct. Ecol.* **32**, 71–82 (2018).
37. Kirsten, M. et al. Iron oxides and aluminous clays selectively control soil carbon storage and stability in the humid tropics. *Sci. Rep.* **11**, 5076 (2021).
38. Zhang, Y. et al. Land cover change-induced decline in terrestrial gross primary production over the conterminous United States from 2001 to 2016. *Agric. For. Meteorol.* **308**, 108609 (2021).
39. Wu, D. et al. Evaluation of CMIP5 earth system models for the spatial patterns of biomass and soil carbon turnover times and their linkage with climate. *J. Clim.* **31**, 5947–5960 (2018).
40. Li, Y. et al. Deforestation-induced climate change reduces carbon storage in remaining tropical forests. *Nat. Commun.* **13**, 1964 (2022).
41. Peng, S. et al. Sensitivity of land-use change emission estimates to historical land-use and land-cover mapping. *Glob. Biogeochem. Cycle* **31**, 626–643 (2017).
42. Jain, A. K. et al. CO_2 emissions from land-use change affected more by nitrogen cycle, than by the choice of land-cover data. *Glob. Change Biol.* **19**, 2893–2906 (2013).
43. Meiyappan, P. & JAIN, A. K. Three distinct global estimates of historical land-cover change and land-use conversions for over 200 years. *Front. Earth Sci.* **6**, 122–139 (2012).
44. Brovkin, V. et al. Effect of anthropogenic land-use and land-cover changes on climate and land carbon storage in CMIP5 projections for the twenty-first century. *J. Clim.* **26**, 6859–6881 (2013).
45. Reick, C. H. et al. Representation of natural and anthropogenic land cover change in MPI-ESM. *J. Adv. Model. Earth Syst.* **5**, 459–482 (2013).
46. Luo, Y. et al. Toward more realistic projections of soil carbon dynamics by Earth system models. *Glob. Biogeochem. Cycle* **30**, 40–56 (2016).

47. Tao, F. et al. Microbial carbon use efficiency promotes global soil carbon storage. *Nature* **618**, 981–985 (2023).
48. Koven, C. D. et al. Controls on terrestrial carbon feedbacks by productivity versus turnover in the CMIP5 Earth System Models. *Biogeosciences* **12**, 5211–5228 (2015).
49. Teuling, A. J. et al. Climate change, reforestation/afforestation, and urbanization impacts on evapotranspiration and streamflow in Europe. *Hydrol. Earth Syst. Sci.* **23**, 3631–3652 (2019).
50. He, Y. et al. Radiocarbon constraints imply reduced carbon uptake by soils during the 21st century. *Science* **353**, 1419–1424 (2016).
51. Hansen, M. C. et al. High-resolution global maps of 21st-century forest cover change. *Science* **342**, 850–853 (2013).
52. He, L. & Xu, X. Mapping soil microbial residence time at the global scale. *Glob. Change Biol.* **27**, 6484–6497 (2021).
53. Chen, S. et al. Temporal and spatial variations in the mean residence time of soil organic carbon and their relationship with climatic, soil and vegetation drivers. *Glob. Planet. Change* **195**, 103359 (2020).
54. Veldkamp, E. et al. Deforestation and reforestation impacts on soils in the tropics. *Nat. Rev. Earth Environ.* **1**, 590–605 (2020).
55. Lemenih, M., Karltun, E. & Olsson, M. Soil organic matter dynamics after deforestation along a farm field chronosequence in southern highlands of Ethiopia. *Agric. Ecosys. Environ.* **109**, 9–19 (2005).
56. Hurtt, G. C. et al. Harmonization of land-use scenarios for the period 1500–2100: 600 years of global gridded annual land-use transitions, wood harvest, and resulting secondary lands. *Clim. Change* **109**, 117 (2011).
57. Chini, L. et al. Land-use harmonization datasets for annual global carbon budgets. *Earth Syst. Sci. Data* **13**, 4175–4189 (2021).
58. Jung, M. et al. Exploiting synergies of global land cover products for carbon cycle modeling. *Remote Sens. Environ.* **101**, 534–553 (2006).
59. Friedlingstein, P. et al. Global carbon budget 2020. *Earth Syst. Sci. Data* **12**, 3269–3340 (2020).
60. Sitch, S. et al. Recent trends and drivers of regional sources and sinks of carbon dioxide. *Biogeosciences* **12**, 653–679 (2015).
61. Wei, N. et al. Nutrient limitations lead to a reduced magnitude of disequilibrium in the global terrestrial carbon cycle. *Journal of Geophysical Research: Biogeosciences* **127**, e2021JG006764 (2022).
62. Wei, N. & Xia, J. Robust projections of increasing land carbon storage in boreal and temperate forests under future climate change scenarios. *One Earth* **7**, 88–99 (2024).
63. Xia, J. et al. Traceable components of terrestrial carbon storage capacity in biogeochemical models. *Glob. Change Biol.* **19**, 2104–2116 (2013).
64. Keenan, T. F. & Williams, C. A. The terrestrial carbon sink. *Annu. Rev. Environ. Resour.* **43**, 219–243 (2018).
65. Pellegrini, A. F. et al. Fire effects on the persistence of soil organic matter and long-term carbon storage. *Nat. Geosci.* **15**, 5–13 (2022).

Acknowledgements

This work was supported by the National Key Research and Development Program of China (2024YFF1306504) and the National Natural Science Foundation of China (31602004). We extend our sincere gratitude to the China Scholarship Council for financial support, and to all the modeling groups from MsTMIP, LUMIP, and TRENDY version 9, as listed in Supplementary Tables 1–3, for sharing the datasets.

Author contributions

C.G.: Conceptualization, data retrieval, formal analysis, draft, and funding acquisition. N.W.: Conceptualization, formal analysis, and draft. C.F.: Data retrieval, formal analysis, and review. H.X.: Data retrieval and review. H.L.: Data retrieval, visualization, and review. F.T.: Data retrieval and review. L.J.: Data retrieval and review. J.X.: Data retrieval and review. S.S.: Data retrieval and review. Y.L.: Conceptualization, review, and supervision.

Competing interests

The authors declare no competing interests. Lifen Jiang is an Editorial Board Member for *Communications Earth & Environment*, but was not involved in the editorial review of, nor the decision to publish this article.

Additional information

Supplementary information The online version contains supplementary material available at https://doi.org/10.1038/s43247-026-03312-6.

Correspondence and requests for materials should be addressed to Ning Wei.

Peer review information *Communications Earth and Environment* thanks the anonymous reviewers for their contribution to the peer review of this work. Primary handling editors: Somaparna Ghosh [A peer review file is available].